Numerical investigation of third-order resonant interactions between two gravity wave trains in deep water

Jian-Jian Xie,[1] Yuxiang Ma ⬤,[1,*] Guohai Dong,[1] and Marc Perlin ⬤[2]

[1]*State Key Laboratory of Coastal and Offshore Engineering, Dalian University of Technology, Dalian 116023, China*

[2]*Department of Ocean Engineering, Texas A&M University, College Station and Galveston, Texas 77554, USA*

The resonant interactions between two gravity wave trains in deep water are studied numerically using a three-dimensional (3D) nonhydrostatic free surface flow model. After model validation, four cases of resonant interactions are simulated and analyzed to study the effect of the primary waves' steepness on the evolutions of the tertiary resonant wave, 3D wave patterns, and velocity profiles. It is found that for primary waves with small steepness, the theories of Longuet-Higgins [J. Fluid Mech. **12**, 321 (1962)] predict well the growth of the resonant wave, that the crest and trough lines of wave patterns are basically straight and regular, and that the linear wave theory roughly estimates well the velocity profiles. For primary waves with moderate steepness, the applicable distance of Longuet-Higgins's theory decreases with an increase of the primary waves' nonlinearity. At greater distances, the growth of the resonant wave is smaller in comparison to Longuet-Higgins's predictions. Strong resonant interactions can lead to the *bending and then splitting of crests and troughs*. The curvatures of the crests and troughs increase with an increase of the primary waves' steepness and the resonant wave's propagation distance. For primary waves with small steepness, the crest and trough lines will eventually split, as long as the propagation distance is sufficiently large. The crest line is split into a longer segment with a larger wave crest and a shorter one with a smaller wave crest. With an increase of the primary waves' nonlinearity, the maximum nondimensionalized wave crest down-wave is found to be larger and more peaked, and its occurrence is earlier, which precisely corresponds to the separated larger wave crest. Meanwhile, the intense resonant and the subsequent quasiresonant interactions have such a significant influence on the velocity profiles that the velocity fields cannot be predicted from the linear predictions.

I. INTRODUCTION

In the retrospective narrative of O. M. Phillips [1], he theoretically reviewed the interactions between two deep-water gravity waves with arbitrary wave-number vectors on the horizontal plane and noted that there were only bound harmonics at second order, whose amplitudes remained forever small in comparison to those of the primary waves. While to the third-order approximation, under certain conditions the amplitude of a third wave, if initially zero, would grow linearly with time. The elaborate theoretical derivations of this work are from Phillips [2], which uncovered the mechanism of nonlinear resonant interaction between two or more progressive gravity wave trains in deep water. Subsequently, the resonance theory in deep-water gravity waves was developed considerably by Longuet-Higgins [3], Benney [4], Hasselmann [5–7], and Bretherton [8] to mention but a few.

---

*yuxma@126.com

The study of resonance mechanisms is of fundamental importance as resonant interactions between different wave components lead to redistribution of energy in a gravity wave spectrum. Hasselmann [5–7] obtained the rate of transfer of energy within a continuous wave spectrum due to four-wave resonant interactions and found that the modification of the wave spectrum by this mechanism should be appreciable. By means of direct numerical simulations of random surface gravity waves in deep water, Tanaka [9] revealed that four-wave resonant interactions control the evolution of the spectrum at every instant of time, whereas nonresonant interactions do not contribute significantly even during short-term evolution. Gibson and Swan [10] investigated the physical mechanisms that govern the evolution of unidirectional and directional focused waves. It is discovered that the formation of a focused wave event involves significant changes to the underlying wave spectrum and these changes are mainly due to the third-order resonant interactions, which are capable of altering not only the amplitude of wave components but also their relative phasing. Onorato *et al.* [11] and Janssen [12] studied the statistical properties of unidirectional random waves and revealed that the modulational instability (i.e., a third-order quasiresonant interaction process), can be responsible for the occurrence of large amplitude waves. As is evident, resonant interaction has a profound influence on the evolution of gravity waves through the significant energy transfer among dominant wave trains.

The earliest verifications of the resonance mechanism were conducted by Longuet-Higgins and Smith [13] and McGoldrick *et al.* [14], considering resonant interactions between two perpendicular gravity wave trains in a small wave tank. The initial growth of the generated resonant wave was identified to be in the manner predicted by Longuet-Higgins [3]. These studies effectively dispelled the initial skepticism of the importance of nonlinear resonant interactions. Then Tomita [15] conducted similar experiments in a large wave tank and investigated both the initial and long-term evolution of the resonant wave. It was shown that for primary waves with small amplitudes, the long fetch behavior of the resonant wave was essentially straight and showed good consistency with the theory of Longuet-Higgins [3]. On the other hand, for primary waves with increased amplitudes, the growth of the resonant wave was small and could be explained better by the Zakharov theory. Recently, Bonnefoy *et al.* [16] extended previous experimental studies from perpendicular gravity waves to oblique gravity waves; the growth of the resonant wave was again verified to agree well with the predictions of Longuet-Higgins [3]. Bonnefoy *et al.* [17] increased the steepness of the primary waves in Ref. [16] and found that new resonant wave components were generated as a result of new four-wave interactions involving the resonant wave and primary waves, which were measured and explained by means of the Zakharov theory.

Although there are experimental studies of resonant interactions between two gravity wave trains in deep water, they concentrate on the spatial evolution of the generated resonant wave through the surface elevations collected from a finite number of distributed wave gauges. Likely due to the difficulties in data acquisition and visual observation, the effect of the third-order resonant interaction on three-dimensional (3D) wave patterns and velocity profiles is rarely mentioned. It is well known that because of four-wave quasiresonance, nonlinear wave groups would become asymmetric in the propagation direction and deform like a crescent [18,19]. So Fujimoto *et al.* [20] recently examined the averaged wave patterns of two observed freak waves in the northwest Pacific Ocean to estimate the impact of four-wave quasiresonance in the formation of a freak wave in deep water. This study implies that if the wave characteristics of exact resonant interaction could be acquired, they may be used to estimate the impact of the four-wave exact resonance in the nonlinear evolutions of water waves. Hence, the effect of the third-order resonant interaction on the evolution of three-dimensional wave patterns and velocity profiles is needed to explore to enrich our understanding of the resonance mechanism. This is pursued in the present study.

By considering the resonant interactions between two gravity wave trains in deep water, Longuet-Higgins [3] provided an explicit expression for the growth of the resonant wave and it has been effectively used to validate previous experimental results for the initial growth of the resonant wave. Bonnefoy *et al.* [16] defined this early stage as the nonlinear propagation distance of the resonant wave less than 1. Are the predictions of Longuet-Higgins [3] always accurate and applicable as long

as this early stage condition is satisfied? This question is another motivation of the present study. As expected and as mentioned above, the theories of Longuet-Higgins [3] predict well the growth of the resonant wave in a long fetch for primary waves with small amplitude in Tomita's experiment. However, it will no longer be accurate if the primary wave's steepness is increased [15].

The rapid development of mathematical techniques and computer power has led to the increasing popularity of numerical methods. In comparison to physical experiments, numerical simulations are more economical and more convenient to implement. In addition, the surface elevations, velocity profiles and three-dimensional wave patterns can be acquired easily without operational or observational difficulties, and the range of the input wave parameters is not limited by experimental constraints. Hence, numerical simulations of the third-order resonant interactions between two gravity wave trains with a fully nonlinear, highly accurate and computationally efficient numerical model is favored, and this is the research tool used in the present study.

For numerical simulation of 3D nonlinear wave evolution, high computational efficiency is desirable, which partly accounts for the widespread use of Schrödinger-type equations and the higher-order spectral method [21–25]. Since the 1990s, continuous efforts have focused on developing nonhydrostatic free surface flow models for simulating water waves. The increasing popularity of this kind of model is due primarily to the following: (1) under the assumption that the free surface is single-valued for all abscissa values, the surface elevation can be efficiently calculated without additional tracking techniques [26–28]; (2) the implementation of the Keller-box scheme enforces the zero pressure boundary condition at the exact free surface, and allows for the use of a small number of vertical layers to obtain accurate dispersion (which further improves the computational efficiency for large-scale wave transformation simulations) [26–28]; and (3) momentum conservation schemes or shock-capturing schemes permit the prediction of discontinuous flows [26,29,30]. In view of these advantages, a nonhydrostatic model based on the Navier-Stokes equations is adopted herein.

In the present study, a fully nonlinear and highly accurate 3D nonhydrostatic model developed by Ai *et al.* [27] and Ai and Jin [30] is utilized to simulate the resonant interactions between two gravity wave trains in deep water. The performance of this model has been demonstrated previously by simulating the process of wave breaking and run-up, and by simulating the nonlinear evolution of two- and three-dimensional focusing wave groups and unidirectional random waves [30–32]. A brief introduction to the third-order resonance theories of surface gravity waves is given in Sec. II, followed by an introduction to the numerical model in Sec. III. In Sec. IV, the validation of the numerical model is demonstrated first. Then, four cases of resonant interactions are simulated to study the effect of the primary waves' steepness on the evolutions of the resonant wave, three-dimensional wave patterns and velocity profiles. The concluding remarks are given in Sec. V.

II. RESONANCE THEORY

In the third-order gravity wave approximation, it is possible for a transfer of energy to occur from three primary waves (of wave-number vectors $\mathbf{k}_1$, $\mathbf{k}_2$, and $\mathbf{k}_3$) to a fourth wave (of wave-number vector $\mathbf{k}_4$) in such a way that the amplitude of the fourth wave, if initially zero, grows linearly with time [2]. The condition for this is

$$\mathbf{k}_1 + \mathbf{k}_2 = \mathbf{k}_3 + \mathbf{k}_4, \quad \omega_1 + \omega_2 = \omega_3 + \omega_4, \tag{1}$$

where the angular frequency ω_i and the magnitude of the wave number $|\mathbf{k}_i|$ are related by the linear dispersion relation for a free wave in deep water, i.e., $\omega_i = \sqrt{g|\mathbf{k}_i|}$ ($i = 1, 2, 3, 4$).

For simplification, many subsequent theoretical and experimental studies are based on the assumption of a degenerate case, i.e., two of the primary wave-number vectors are equal, say, $\mathbf{k}_1 = \mathbf{k}_2$, so that the resonance conditions Eq. (1) becomes

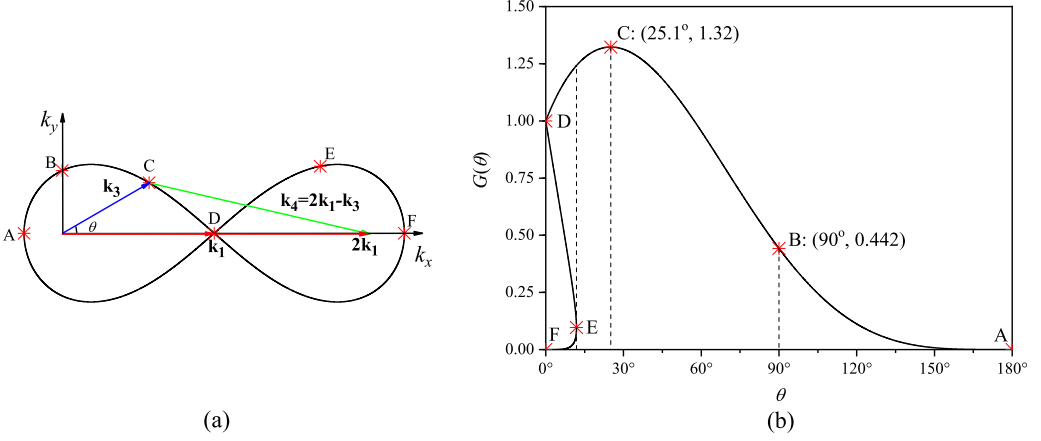$$2\mathbf{k}_1 = \mathbf{k}_3 + \mathbf{k}_4, \quad 2\omega_1 = \omega_3 + \omega_4. \tag{2}$$

FIG. 1. (a) Figure-of-eight resonance loop. (b) The coupling coefficient G vs θ.

With $\mathbf{k}_1$ fixed, the locus of $\mathbf{k}_3$ is a figure-of-eight loop as shown in Fig. 1(a), i.e., for any point on this curve, the wave-number vector set $\{2\mathbf{k}_1, \mathbf{k}_3, \mathbf{k}_4\}$ satisfies Eq. (2).

Under the simplification of $\mathbf{k}_1 = \mathbf{k}_2$, Phillips [2] estimated the order of magnitude of the interaction. With an improved analysis, Longuet-Higgins [3] produced an exact expression for the coupling coefficient $G(r, \theta)$ and gave the amplitude of the resonant wave as

$$a_4 = \varepsilon_1^2 \varepsilon_3 d G(r, \theta), \tag{3}$$

where a_4 is the amplitude of the generated resonant wave, $\varepsilon_i = k_i a_i$ is the wave steepness of the primary wave $\mathbf{k}_i$ ($i = 1, 3$), d is the propagation distance of the resonant wave $\mathbf{k}_4$, $r = f_1/f_3$ is the frequency ratio, and θ denotes the crossing angle between $\mathbf{k}_1$ and $\mathbf{k}_3$. It can be seen that for a fixed coupling coefficient, the amplitude of the resonant wave grows linearly with its propagation distance.

The expression of $G(r, \theta)$ can be found in Longuet-Higgins [3] and is rewritten here for convenience as

$$G(r, \theta) = \frac{(2r-1)(1+\cos\theta)}{2r^3} \left[(r-1)(r^2+1-\sqrt{r^4+1-2r^2\cos\theta}) + \frac{r(1+\cos\theta)}{2} \right.$$
$$\left. - \frac{2r(r-1)(2r-1)(\sqrt{r^4+1-2r^2\cos\theta}+\cos\theta-r^2)}{(r-1)^2 - \sqrt{r^4+1-2r^2\cos\theta}} \right], \tag{4}$$

where r and θ are related through $\cos\theta = 2r^2(1/r - 1)^3 + 2r - r^2$. Thus $G(r, \theta)$ may also be defined as a function of $G(r)$ or $G(\theta)$. Clearly, from Eq. (4), the coupling coefficient G is seen to be an even function of θ. Figure 1(b) depicts the curve of $G(\theta)$ for $\theta \geqslant 0$, i.e., in the upper loop of Fig. 1(a). The points from A to D correspond to the locus of $\mathbf{k}_3$ in the left-hand loop, and the points from D to F correspond to the right-hand loop. Since the locus of $\mathbf{k}_3$ is not single valued with respect to θ, $G(\theta)$ is double or triple valued for $\theta \leqslant 11.85°$ (corresponding to point E). It is shown that the maximum value $G_{\max} = 1.32$ is achieved at $\theta = 25.1°$, which indicates where the growth rate of the resonant wave is the greatest and the resonant interactions are the most intense. The previous experimental studies involving two perpendicular wave trains correspond to point B [13–15], while involving two oblique wave trains with $G_{\max}$ correspond to point C [16,17]. In Ref. [16], the resonant experiments were conducted over a wide range of θ with $-15° \leqslant \theta \leqslant 40°$.

It is worth noting that the third-order theoretical prediction in Eq. (3) is only valid for the initial growth of the resonant wave. Otherwise, the energy of the resonant wave would keep growing, which is physically impossible. In particular, the growth rate of the resonant wave is derived under

the assumption that the primary waves' amplitudes are unaffected by the amplitude growth of the resonant wave, so that Eq. (3) remains valid as long as $a_4 \ll a_1$ and $a_4 \ll a_3$.

III. NUMERICAL MODEL

A. Governing equations

A fully nonlinear and highly accurate 3D nonhydrostatic free surface flow model [27,30] is employed in this study. One significant feature of the nonhydrostatic model is that the total pressure p is split into a hydrostatic part and a nonhydrostatic part, $p = \rho g(\eta - z) + q$, so the incompressible Navier-Stokes equations can be expressed as

$$\frac{\partial u}{\partial x} + \frac{\partial v}{\partial y} + \frac{\partial w}{\partial z} = 0, \tag{5}$$

$$\frac{\partial u}{\partial t} + \frac{\partial uu}{\partial x} + \frac{\partial uv}{\partial y} + \frac{\partial uw}{\partial z} = -g\frac{\partial \eta}{\partial x} - \frac{1}{\rho}\frac{\partial q}{\partial x} + \nu\left(\frac{\partial^2 u}{\partial x^2} + \frac{\partial^2 u}{\partial y^2} + \frac{\partial^2 u}{\partial z^2}\right), \tag{6}$$

$$\frac{\partial v}{\partial t} + \frac{\partial uv}{\partial x} + \frac{\partial vv}{\partial y} + \frac{\partial vw}{\partial z} = -g\frac{\partial \eta}{\partial y} - \frac{1}{\rho}\frac{\partial q}{\partial y} + \nu\left(\frac{\partial^2 v}{\partial x^2} + \frac{\partial^2 v}{\partial y^2} + \frac{\partial^2 v}{\partial z^2}\right), \tag{7}$$

$$\frac{\partial w}{\partial t} + \frac{\partial uw}{\partial x} + \frac{\partial vw}{\partial y} + \frac{\partial ww}{\partial z} = -\frac{1}{\rho}\frac{\partial q}{\partial z} + \nu\left(\frac{\partial^2 w}{\partial x^2} + \frac{\partial^2 w}{\partial y^2} + \frac{\partial^2 w}{\partial z^2}\right), \tag{8}$$

where $u(x, y, z, t)$, $v(x, y, z, t)$, and $w(x, y, z, t)$ are the velocity components in the x, y and z directions; t is the time; $\eta(x, y, t)$ is the free surface elevation; $q(x, y, z, t)$ is the nonhydrostatic pressure component; ρ ($=10^3$ kg/m^3) is the constant density; g ($=9.81$ m/s^2) is the gravitational acceleration, and ν ($=10^{-6}$ m^2/s) is the kinematic viscosity.

Another significant feature of the nonhydrostatic model is the single-valued assumption of the surface elevations $\eta(x, y, t)$ in the horizontal plane. Integrating the continuity equation over the vertical water volume and combining the following kinematic boundary conditions

$$\frac{\partial \eta}{\partial t} + u\frac{\partial \eta}{\partial x} + v\frac{\partial \eta}{\partial y} = w|_{z=\eta}, \tag{9}$$

$$-u\frac{\partial h}{\partial x} - v\frac{\partial h}{\partial y} = w|_{z=-h}, \tag{10}$$

the governing equation of the free surface movement can be obtained as

$$\frac{\partial \eta}{\partial t} + \frac{\partial}{\partial x}\int_{-h}^{\eta} u\,dz + \frac{\partial}{\partial y}\int_{-h}^{\eta} v\,dz = 0. \tag{11}$$

B. Numerical algorithms

This model is built on the horizontal Cartesian grid framework and vertical boundary-fitted coordinate system. A two-step projection method, known as pressure correction method, is utilized to solve the governing equations. The overall numerical algorithms consist of the following three steps.

In the first step, an intermediate velocity field $\mathbf{U}^{n+1/2}$ is solved from the momentum equations containing the nonhydrostatic pressure component at the previous time level as

$$\frac{u^{n+1/2} - u^n}{\Delta t} = -\left(\frac{\partial uu}{\partial x} + \frac{\partial uv}{\partial y} + \frac{\partial uw}{\partial z}\right)^n - g\frac{\partial \eta^n}{\partial x} - \frac{1}{\rho}\frac{\partial q^n}{\partial x} + \nu\left(\frac{\partial^2 u}{\partial x^2} + \frac{\partial^2 u}{\partial y^2} + \frac{\partial^2 u}{\partial z^2}\right)^n, \tag{12}$$

where the superscript n denotes the time step. The solution procedures for $v^{n+1/2}$ and $w^{n+1/2}$ are similar and so omitted. In the following steps, the solutions for v^{n+1} and w^{n+1} are omitted as well.
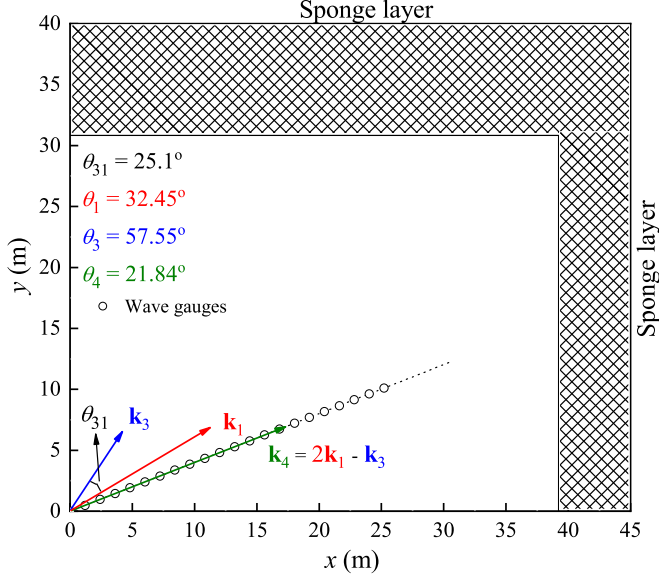
FIG. 2. Sketch of the plan view of the numerical wave tank where $\mathbf{k}_1$ and $\mathbf{k}_3$ represent two primary waves, and $\mathbf{k}_4 = 2\mathbf{k}_1 - \mathbf{k}_3$ denotes the generated resonant wave.

In the second step, the new velocity field $\mathbf{U}^{n+1}$ is updated by including the nonhydrostatic pressure component at the new time level as

$$\frac{u^{n+1} - u^n}{\Delta t} = -\left(\frac{\partial uu}{\partial x} + \frac{\partial uv}{\partial y} + \frac{\partial uw}{\partial z}\right)^n - g\frac{\partial \eta^n}{\partial x} - \frac{1}{\rho}\frac{\partial q^{n+1}}{\partial x} + \nu\left(\frac{\partial^2 u}{\partial x^2} + \frac{\partial^2 u}{\partial y^2} + \frac{\partial^2 u}{\partial z^2}\right)^n. \quad (13)$$

Subtracting $\mathbf{U}^{n+1/2}$ from $\mathbf{U}^{n+1}$, one obtains

$$u^{n+1} = u^{n+1/2} - \frac{\Delta t}{\rho}\frac{\partial \Delta q}{\partial x}, \quad (14)$$

where $\Delta q = q^{n+1} - q^n$. The divergence-free velocity field $\mathbf{U}^{n+1}$ leads to the Poisson equation for the nonhydrostatic pressure correction term, Δq, which could be solved by preconditioned conjugated gradient method. Once Δq is calculated, both q^{n+1} and $\mathbf{U}^{n+1}$ can be determined.

In the last step, substituting the updated velocity field $\mathbf{U}^{n+1}$ into a discretized form of Eq. (11), the new free surface elevation η^{n+1} is subsequently calculated.

Detailed spatial discretizations and variable definitions can be found in Refs. [27,30].

C. Numerical wave tank

Bonnefoy *et al.* [16] conducted an experiment to observe the growth of the resonant wave in a rectangular wave tank ($50 \times 30 \times 5$ m) at Ecole Centrale de Nantes. Two primary waves were mechanically generated by a flap-type wavemaker along the width direction and to avoid spurious reflections on the sidewalls, the Dalrymple method [33] was used to control the motions of the wavemaker. This method yields a finite zone of the quasiuniform wave field as shown by the gray zone in Fig. 3(a) in Ref. [16].

To prevent the sidewall reflections and to maximize the interaction zone, a 3D numerical wave tank with two adjacent wavemaker boundaries is established. A plan view sketch of the wave tank is shown in Fig. 2, where two regular gravity waves $\mathbf{k}_1$ and $\mathbf{k}_3$ are generated from the x and y axes boundaries simultaneously. For consistency with previous experimental studies, linear wave theory

is used to generate the wavemaker conditions. Thus, the incident waves are generated by specifying the inlet velocity components as follows:

$$u(x, y, z, t) = \sum_{i=1,3} a_i \omega_i \frac{\cosh k_i(z + h)}{\sinh k_i h} \cos \left(\frac{\pi}{2} + k_i x \cos \theta_i + k_i y \sin \theta_i - \omega_i t \right) \cos \theta_i,$$

$$v(x, y, z, t) = \sum_{i=1,3} a_i \omega_i \frac{\cosh k_i(z + h)}{\sinh k_i h} \cos \left(\frac{\pi}{2} + k_i x \cos \theta_i + k_i y \sin \theta_i - \omega_i t \right) \sin \theta_i, \qquad (15)$$

$$w(x, y, z, t) = \sum_{i=1,3} a_i \omega_i \frac{\sinh k_i(z + h)}{\sinh k_i h} \sin \left(\frac{\pi}{2} + k_i x \cos \theta_i + k_i y \sin \theta_i - \omega_i t \right),$$

in which a_i, ω_i, k_i, and θ_i are the wave amplitude, angular frequency, magnitude of the wave-number vector, and propagation direction of the wave-number vector $\mathbf{k}_i$ ($i = 1, 3$), respectively. Once the crossing angle between $\mathbf{k}_1$ and $\mathbf{k}_3$ is specified, i.e., $\theta_{31} = \theta_3 - \theta_1$, the directions of $\mathbf{k}_1$ and $\mathbf{k}_3$ with respect to the positive x axis are determined to be $\theta_1 = 45° - \theta_{31}/2$ and $\theta_3 = 45° + \theta_{31}/2$. If the resonance conditions Eq. (2) are satisfied, then a tertiary resonant wave $\mathbf{k}_4 = 2\mathbf{k}_1 - \mathbf{k}_3$ would be generated and its amplitude would grow linearly along its propagation direction as predicted by Eq. (3).

The numerical tank is 45 m long, 40 m wide, and 5.0 m deep (i.e., in the x, y, and z directions). At the inflow boundaries, a ramp function $f_i(t) = 0.5[1 + \tanh (2t/T_i - 2)]$, buffering three periods of T_i, is applied to the inlet velocities to prevent initially short waves with relatively large amplitudes. At the outflow boundaries, numerical sponge layers with a width of $3L_1$ and $3L_3$ are embedded at the ($x = 45$ m, y) and (x, $y = 40$ m) boundaries, respectively, to help absorb wave energy and prevent wave reflections, where L_i is the wavelength of $\mathbf{k}_i$ ($i = 1, 3$).

IV. RESULTS AND DISCUSSION

Bonnefoy *et al.* [16] experimentally observed the third-order resonant interactions between two oblique gravity wave trains for $-15° \leqslant \theta_{31} \leqslant 40°$. To validate the present model, the wave parameters are chosen to be consistent with their experiments. Thus $h = 5.0$ m, $f_1 = 0.9$ Hz, $f_3 = 0.715$ Hz, $r = f_1/f_3 = 1.259$, $\theta_{31} = 25.1°$, which are the wave parameters corresponding to the maximum value of the coupling coefficient ($G_{\max} = 1.32$). The sketch of the wave-number vectors of the primary waves $\mathbf{k}_1$, $\mathbf{k}_3$ and the generated resonant wave $\mathbf{k}_4$ is illustrated in Fig. 2.

A. Model validation

In this subsection, both nonresonant and resonant interactions between $\mathbf{k}_1$ and $\mathbf{k}_3$ are simulated to test the reliability of the employed model. Table I lists the wave parameters of five cases to be investigated, where $\varepsilon_i = k_i a_i$ ($i = 1, 3$) denotes the wave steepness of each primary wave. The horizontal grid size $\Delta x = 0.03$ m and $\Delta y = 0.04$ m, and the time step $\Delta t = 0.005$ s are used in the simulations. In the vertical direction, 13 layers are set to discretize the water volume.

TABLE I. Wave parameters of the five cases for model validation, where $h = 5.0$ m.

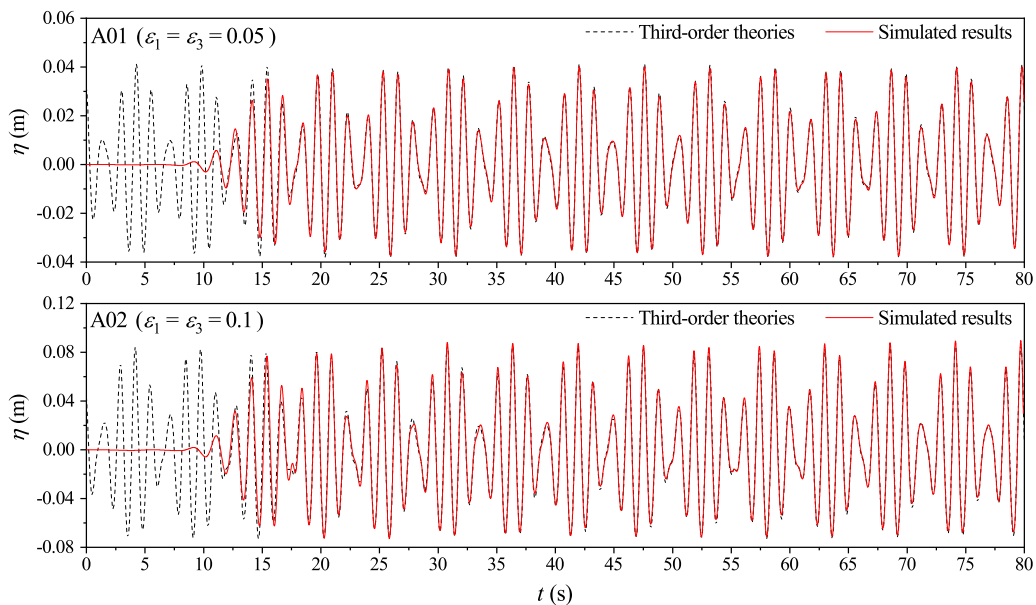| Cases	f_1 (Hz)	f_3 (Hz)	ε_1	ε_3	θ_{31}	$k_1 h$	$k_3 h$
A01	0.9	0.715	0.05	0.05	60°	16.3	10.3
A02	0.9	0.715	0.1	0.1	60°	16.3	10.3
B01	0.9	0.715	0.041	0.05	25.1°	16.3	10.3
B02	0.9	0.715	0.056	0.05	25.1°	16.3	10.3
B03	0.9	0.715	0.068	0.05	25.1°	16.3	10.3

FIG. 3. Comparisons of the surface elevations between the simulated results and the third-order (nonresonant) theories of Madsen and Fuhrman [34] at the location (12 m, 12 m) for A01 and A02, respectively.

In cases A01 and A02, the crossing angle between $\mathbf{k}_1$ and $\mathbf{k}_3$ is set to $\theta_{31} = 60°$ for off-resonance so that the third-order theories of Madsen and Fuhrman [34] for bichromatic bidirectional waves can be used for comparison. Figure 3 compares the surface elevations between the simulated and theoretical results at the location (12 m, 12 m). It can be seen that when the resonance conditions are far from being satisfied, the simulated results agree quite well with previous third-order theories for
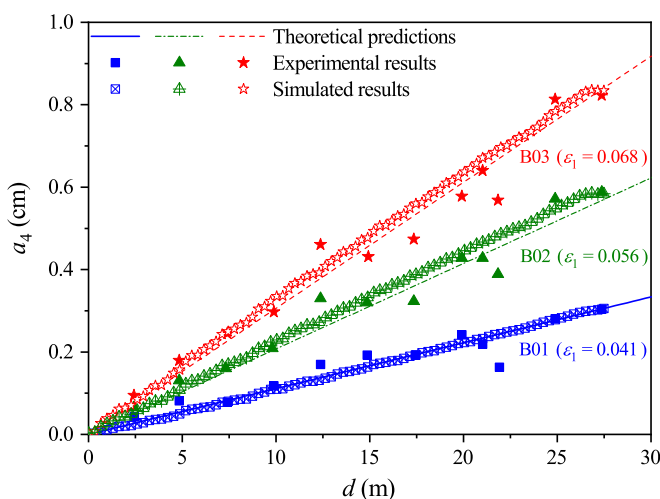
FIG. 4. Comparisons of the generated resonant wave's amplitude for the theoretical predictions of Longuet-Higgins [3], the experimental results of Bonnefoy et al. [16], and the simulated results for B01 (blue), B02 (olive), and B03 (red), respectively.
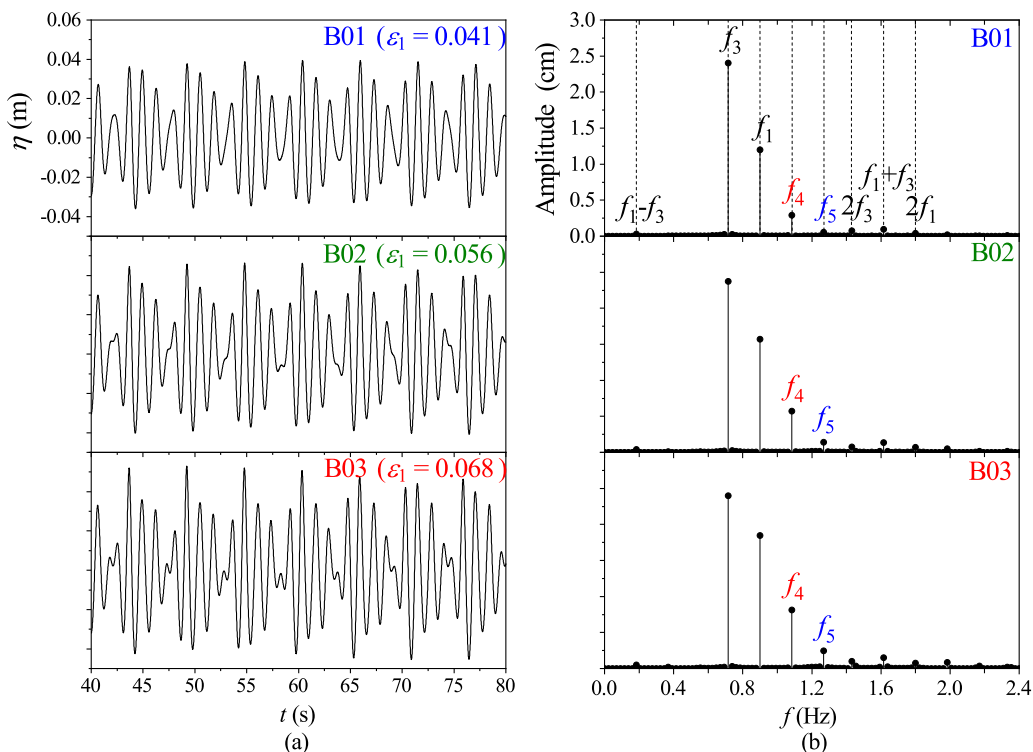
FIG. 5. Time series of the surface elevations and their corresponding amplitude spectra at $d = 25.9$ m ($x = 24$ m, $y = 9.6$ m) for B01, B02, and B03, respectively.

the nonlinear interactions between $\mathbf{k}_1$ and $\mathbf{k}_3$ with small ($\varepsilon = 0.05$) and moderate ($\varepsilon = 0.10$) wave steepness.

In cases B01–B03, the resonant interactions between $\mathbf{k}_1$ and $\mathbf{k}_3$ are simulated. The amplitude growth of the resonant wave $\mathbf{k}_4 = 2\mathbf{k}_1 - \mathbf{k}_3$ is determined and compared with the experimental results of Bonnefoy et al. [16] and the third-order theoretical prediction of Longuet-Higgins [3]. The crossing angle between $\mathbf{k}_1$ and $\mathbf{k}_3$ is set to be $\theta_{31} = 25.1°$ and a series of numerical wave gauges are arranged along the direction of $\mathbf{k}_4$ with $\theta_4 = 21.84°$ to detect the growth of the resonant wave (see Fig. 2). Figure 4 compares the amplitude of the resonant wave a_4 for the previous theoretical predictions, experimental results and the present simulated results, where $d = x_0/\cos\theta_4$ is the propagation distance of the resonant wave and x_0 is the x coordinate of the numerical wave gauges. The numerical amplitudes are obtained by applying a fast Fourier transformation (FFT) to the time series of surface elevations at each wave gauge. It is shown that for resonant cases B01–B03, the simulated results agree well with the previous solutions and the amplitude of the resonant wave indeed exhibits a linear growth along its finite propagation distance. These tests again demonstrate the reliability and accuracy of the employed numerical model.

For the resonant cases B01–B03, the simulated surface elevations and their amplitude spectra at $d = 25.9$ m ($x = 24$ m, $y = 9.6$ m) are given in Fig. 5. It can be seen that except for the primary waves, the amplitude of the resonant wave component f_4 ($f_4 = 2f_1 - f_3 = 1.085$ Hz) can be observed to be finite. With an increase of ε_1, the amplitude of the resonant wave component also increases. This is consistent with the theoretical predictions in Eq. (3). Meanwhile, the amplitudes of the bound wave components resulting from self- and mutual-interactions between the two primary waves ($f_1 - f_3, 2f_1, 2f_3, f_1 + f_3$) always remain small. In addition, it is noticed that the amplitude of another wave component $f_5 = 1.27$ Hz, which is also initially zero, exhibits a mild growth

TABLE II. Wave parameters for resonant interactions, where $h = 5.0$ m.

Cases	f_1 (Hz)	f_3 (Hz)	ε_1	ε_3	θ_{31}	θ_1	θ_3
C01	0.9	0.715	0.03	0.03	25.1°	32.45°	57.55°
C02	0.9	0.715	0.05	0.05	25.1°	32.45°	57.55°
C03	0.9	0.715	0.08	0.08	25.1°	32.45°	57.55°
C04	0.9	0.715	0.1	0.1	25.1°	32.45°	57.55°

with the increase of ε_1 and it exceeds that of all the second-order components in case B03. This wave component has been detected by Bonnefoy *et al.* [17] in a case with primary waves of $0.07 \leqslant \varepsilon_1 = \varepsilon_3 \leqslant 0.14$. It can be seen from Fig. 5(b) that f_5 is also generated from the resonant interactions of two primary waves with smaller steepness. As to the cause of its generation, it is discussed in the next subsection.

B. Resonant interactions

The resonance theory of Longuet-Higgins [3] gives only the growth rate of the resonant wave along its propagation distance, while the previous experimental studies mainly concentrated on the evolution of the resonant wave. Due to the difficulties in data acquisition and visual observation, the effect of the third-order resonant interactions on three-dimensional wave patterns and velocity profiles has not yet been discussed. In this subsection, the resonant interactions between $\mathbf{k}_1$ and $\mathbf{k}_3$ are simulated to investigate the effect of the primary waves' steepness on the evolutions of the resonant wave, three-dimensional wave patterns and velocity profiles. The wave parameters are listed in Table II and the numerical parameters are consistent with those in the previous subsection.

Figure 6 presents a comparison of the resonant wave's amplitude between the theoretical predictions of Longuet-Higgins [3] and the present numerical results. It can be seen that for primary waves with a small wave steepness as in C01 and C02 ($\varepsilon = 0.03, 0.05$), the simulated amplitude growth of the resonant wave coincides well with the resonance theory of Longuet-Higgins [3]. On the other hand, for primary waves with a moderate wave steepness as in C03 and C04 ($\varepsilon = 0.08, 0.10$), evident discrepancies appear. Specifically, the numerical and theoretical solutions are consistent
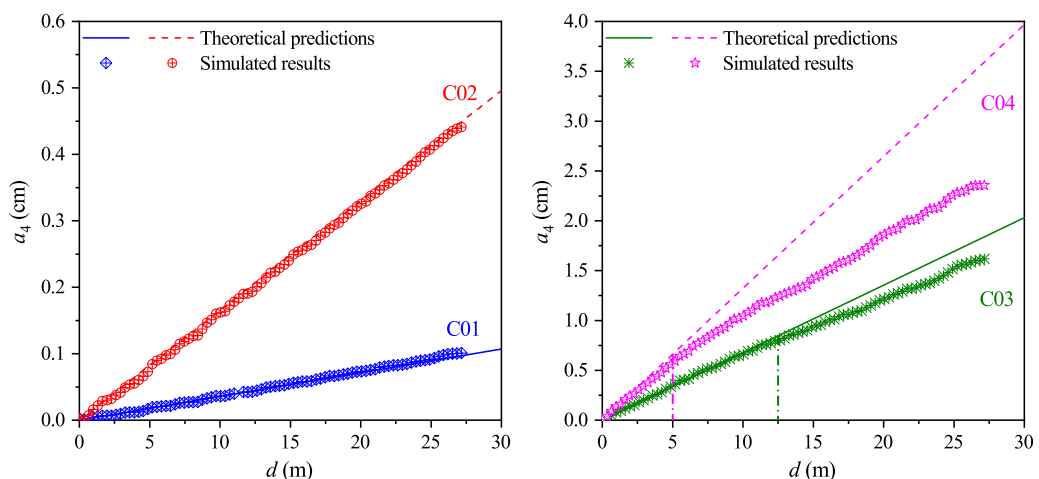

FIG. 6. Comparisons of the resonant wave's amplitude between the theoretical predictions of Longuet-Higgins [3] and the present numerical results for C01 (blue), C02 (red), C03 (olive), and C04 (magenta), respectively.
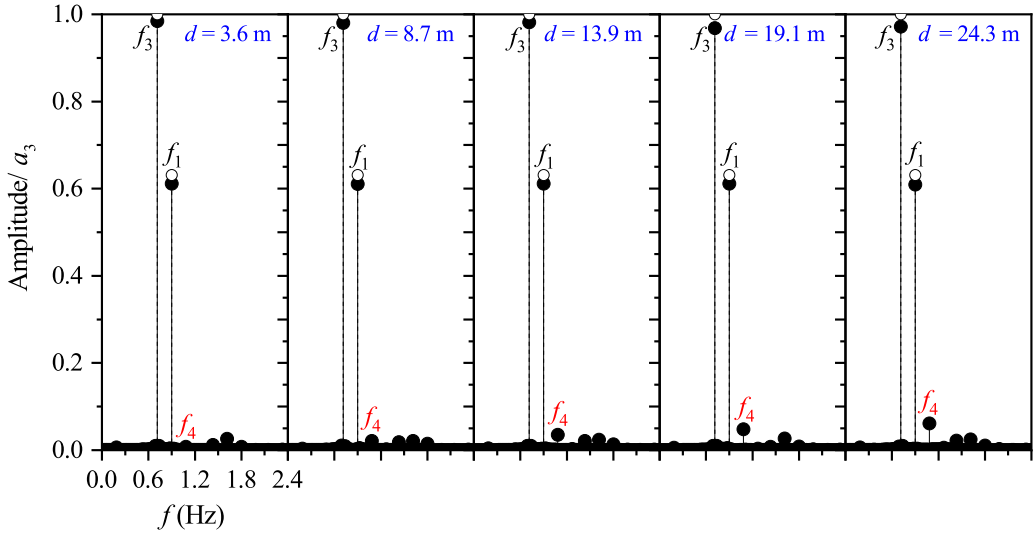
FIG. 7. Amplitude spectra for C01 with $\varepsilon_1 = \varepsilon_3 = 0.03$, where the hollow circles denote the input amplitudes of the primary waves and $a_3 = \varepsilon_3/k_3$.

within only a short propagation distance of $d < 12.5$ m in C03 and within a shorter propagation distance of $d < 5.0$ m in C04. Beyond these d values as indicated by the dash dot lines, the discrepancies become increasingly evident and the third-order theoretical predictions of Longuet-Higgins [3] overestimate the growth of the resonant wave.

To explore the reason for the curve divergences, Figs. 7–10 present the amplitude spectra at different propagation distances of the resonant wave in cases C01–C04, respectively. By comparison, it is found that in C01 and C02, the resonant wave $f_4 = 2f_1 - f_3 = 1.085$ Hz is the only frequency component of which the amplitude grows evidently with its propagation distance, while
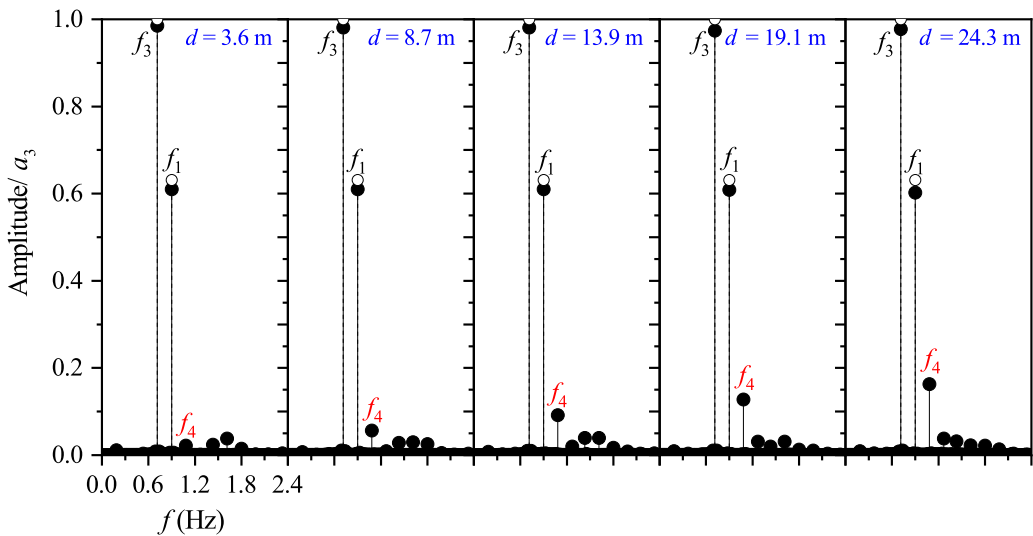

FIG. 8. Amplitude spectra for C02 with $\varepsilon_1 = \varepsilon_3 = 0.05$, where the hollow circles denote the input amplitudes of the primary waves and $a_3 = \varepsilon_3/k_3$.
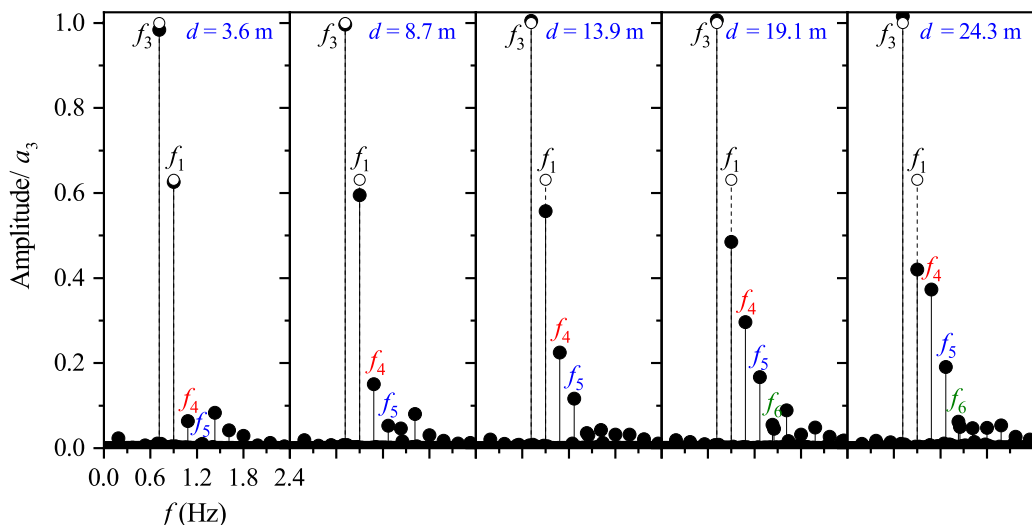
FIG. 9. Amplitude spectra for C03 with $\varepsilon_1 = \varepsilon_3 = 0.08$, where the hollow circles denote the input amplitudes of the primary waves and $a_3 = \varepsilon_3/k_3$.

the amplitudes of the primary waves basically remain unchanged. In C03 and C04, except for the rapid amplitude growth of the resonant wave f_4, the amplitude of another newly generated wave component $f_5 = 1.27$ Hz also exhibits distinct increase. Additionally, a slight amplitude growth of the frequency component $f_6 = 1.455$ Hz is observed as well. Due to transferring energy to these generated wave components, the amplitude of the primary wave $\mathbf{k}_1$ decreases significantly along the propagation direction of the resonant wave. As can be seen, for primary waves with moderate steepness, the resonant interactions are so significant that additional wave components are generated and the amplitude spectrum experiences obvious change. Note that the total energy
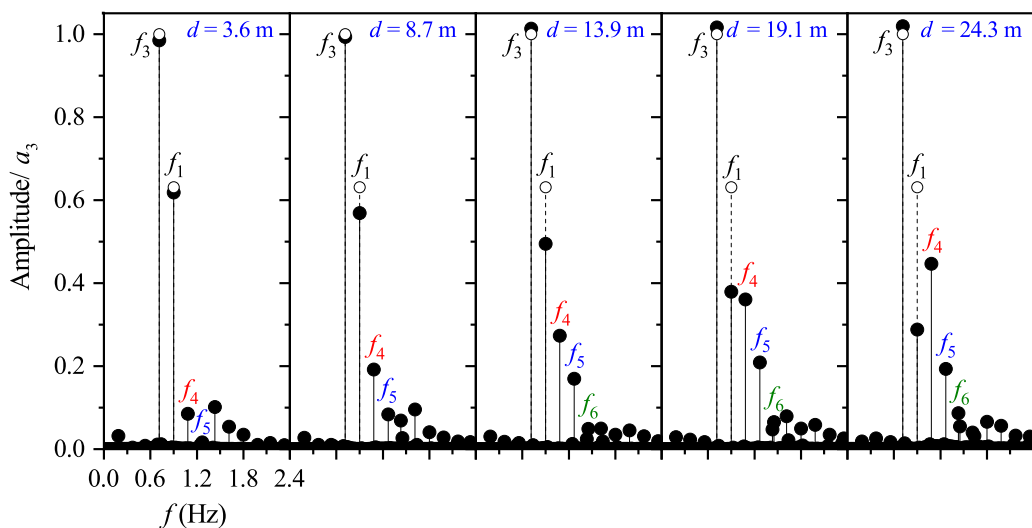

FIG. 10. Amplitude spectra for C04 with $\varepsilon_1 = \varepsilon_3 = 0.10$, where the hollow circles denote the input amplitudes of the primary waves and $a_3 = \varepsilon_3/k_3$.

has been determined for each of the four cases by summing $\rho g a^2/2$ of each wave component, and this value is seen to be constant along the direction of the resonant wave.

As mentioned previously, the resonance theory of Longuet-Higgins [3] was derived using perturbation methods under the assumption that the primary waves' amplitudes are unaffected by the growth of the resonant wave. Therefore, this theory is only valid on the condition that $a_4 \ll a_1$ and $a_4 \ll a_3$. It can be seen from Figs. 7 and 8 that the evolutions of the amplitude spectra in cases C01 and C02 are in accord with this assumption, so that the numerical amplitude of the resonant wave coincides well with the theoretical predictions. However, in cases C03 and C04, because of the significant energy transfer, the amplitude of the primary wave $\mathbf{k}_1$ reduces so that the resonant wave's amplitude becomes comparable to or even exceeds it at $d = 24.3$ m as shown in Figs. 9 and 10. Apparently, the evolutions of the amplitude spectra in C03 and C04 are inconsistent with the assumption of Eq. (3), leading to the discrepancies shown in Fig. 6. This is as expected for moderate wave steepness.

Due to the preconditions that $a_4 \ll a_1$ and $a_4 \ll a_3$, the predictions of Longuet-Higgins [3] are valid only in the early stage of resonant interactions. Bonnefoy et al. [16] defined the early stage as the nonlinear distance $k_4 d \varepsilon^2 < 1$, where ε denotes the steepness of the primary waves, k_4 and d are the wave number and propagation distance of the resonant wave, respectively. It was stated in Ref. [16] that for a longer distance or greater steepness, the pumping of the primary wave by the resonant wave and the decrease of the resonant-wave growth were observed. In the present study, the maximum nonlinear distances $k_4 d_{\max} \varepsilon^2$ in C01–C04 are 0.116, 0.322, 0.823, and 1.287, respectively, where $d_{\max} = 27.16$ m. Although the early stage condition is satisfied in C01–C03 and in C04 for $d < 21.11$ m, it is shown from Fig. 6 that the numerical and theoretical solutions are consistent only within $d < 12.5$ m or $k_4 d \varepsilon^2 < 0.379$ in C03, and within $d < 5.0$ m or $k_4 d \varepsilon^2 < 0.237$ in C04. Otherwise, Eq. (3) overestimates the growth of the resonant wave. It is not difficult to see that the propagation distance d or nonlinear distance $k_4 d \varepsilon^2$ of the resonant wave, within which the theory of Longuet-Higgins [3] is accurate, decreases with an increase of the primary waves' nonlinearity. Beyond theses distances, numerical or experimental studies are necessary to supplement this theory.

As indicated in Figs. 9 and 10, except for the rapid amplitude growth of the resonant wave component, f_4, the amplitudes of the frequency components f_5 and f_6 also show visible growth. Figure 11 compares the normalized steepness evolutions of f_4, f_5, and f_6 for the numerical solution of the Zakharov equation, the experimental results of Bonnefoy et al. [17] and the present numerical results in case C04 with $\varepsilon_1 = \varepsilon_3 = 0.10$. It can be seen that for the small nondimensionalized propagation distance of $\mathbf{k}_4$, all the solutions are consistent. As the resonant interactions evolve further, the simulated results show relatively better agreement with the solution of the Zakharov equation. However, overall, the employed numerical model predicts well the dominant energy transfer during the significant resonant interactions between $\mathbf{k}_1$ and $\mathbf{k}_3$.

The amplitude evolutions of the primary wave components and the newly generated wave components f_4, f_5, and f_6 in cases C03 and C04 are shown in Fig. 12. It can be seen that within the finite computational domain, there is continuous energy transfer into the components f_4, f_5, and f_6, and the amplitude of the resonant wave $\mathbf{k}_4$ basically equals that of the primary wave $\mathbf{k}_1$ in C03 at $d = 25.5$ m ($k_4 d \varepsilon^2 = 0.77$) and in C04 at $d = 19.6$ m ($k_4 d \varepsilon^2 = 0.93$). It is noticed that essentially all the energy is supplied by the primary wave $\mathbf{k}_1$. In contrast, the amplitude of the primary wave $\mathbf{k}_3$ is found to be slightly larger down-wave than its initial input value. In the theoretical part of McGoldrick et al. [14], it is stated that the initial growth of the resonant wave component $\mathbf{k}_4$ is accompanied by an increase in the energy density of the $\mathbf{k}_3$ component, both at the expense of the $\mathbf{k}_1$ component. It can be seen from Fig. 12 that the simulated results are supportive of their theoretical descriptions.

The generation of the component $f_4 = 2f_1 - f_3$ is undoubtedly due to the third-order exactly resonant interactions between the primary waves $\mathbf{k}_1$ and $\mathbf{k}_3$. Bonnefoy et al. [17] attributed the formation of f_5 and f_6 to new four-wave quasiresonant interactions among $\mathbf{k}_1$, $\mathbf{k}_3$, and $\mathbf{k}_4$ either in degenerate quartets as $\mathbf{k}_5 = 2\mathbf{k}_4 - \mathbf{k}_1$ and $\mathbf{k}_6 = 2\mathbf{k}_4 - \mathbf{k}_3$, or in general sets as
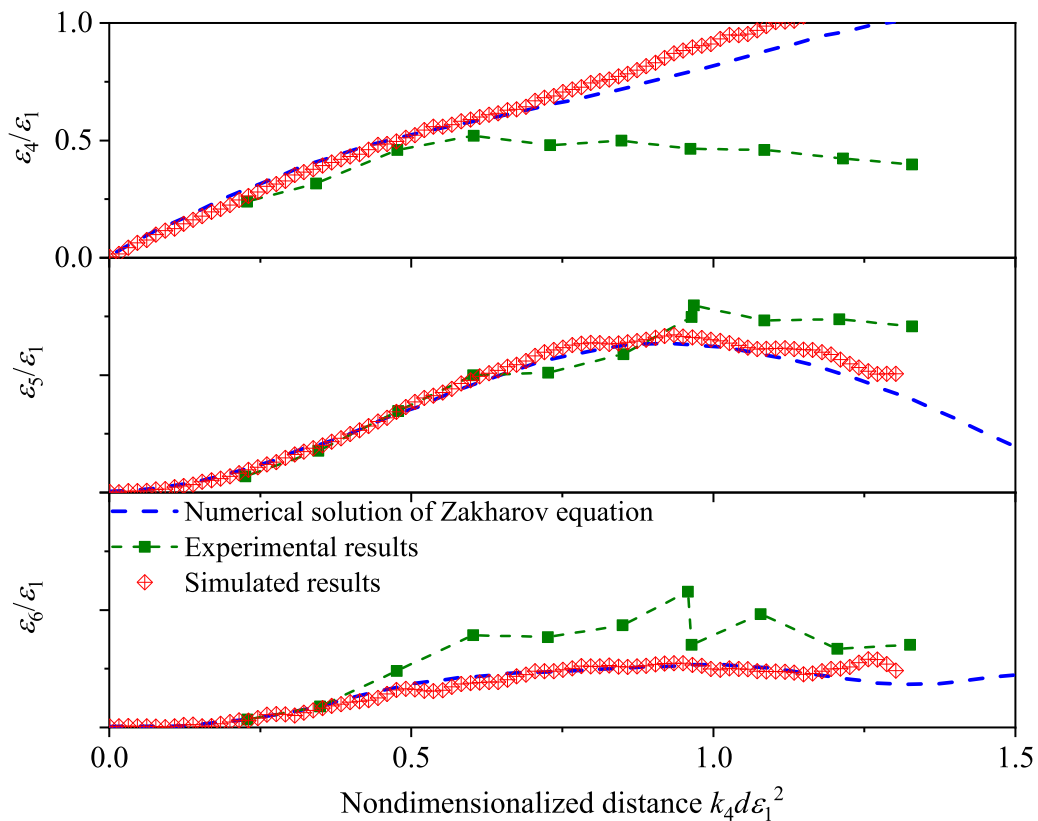
FIG. 11. Normalized steepness evolutions of f_4, f_5, and f_6 with nondimensionalized propagation distances of the resonant wave for C04.
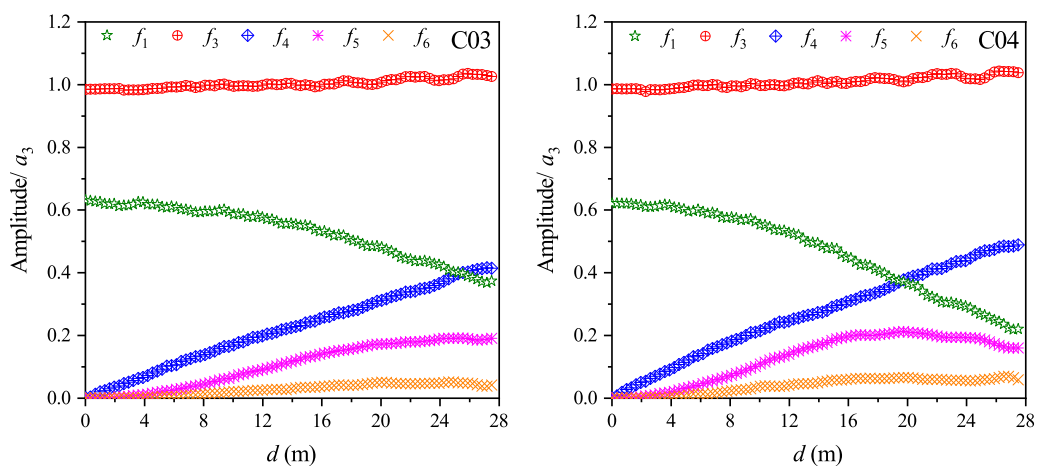

FIG. 12. Amplitude evolutions of the frequency components f_i ($i = 1, 3, 4, 5, 6$) along the propagation direction of the resonant wave $\mathbf{k}_4$ for C03 and C04, respectively.
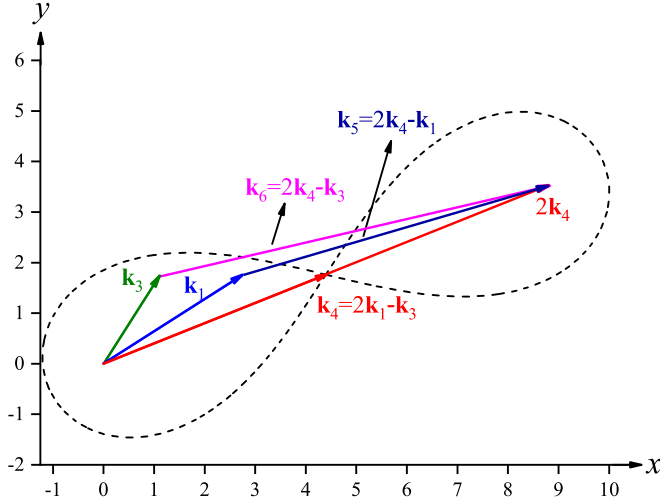
FIG. 13. Wave-number vectors involved in the degenerate quasiresonant interactions.

$\mathbf{k}_5 = \mathbf{k}_1 + \mathbf{k}_4 - \mathbf{k}_3$ and $\mathbf{k}_6 = \mathbf{k}_4 + \mathbf{k}_5 - \mathbf{k}_1$. The wave-number vectors involved in the degenerate quasiresonant interactions are shown in Fig. 13, where the resonant loop with respect to $\mathbf{k}_4$ is plotted for reference. Obviously, neither the wave-number vector set $\{2\mathbf{k}_4, \mathbf{k}_1, \mathbf{k}_5\}$ nor the set $\{2\mathbf{k}_4, \mathbf{k}_3, \mathbf{k}_6\}$ satisfies the resonance conditions Eq. (2). Since $\mathbf{k}_4 = 2\mathbf{k}_1 - \mathbf{k}_3$, the general sets $\{\mathbf{k}_1, \mathbf{k}_4, \mathbf{k}_3, \mathbf{k}_5\}$ and $\{\mathbf{k}_4, \mathbf{k}_5, \mathbf{k}_1, \mathbf{k}_6\}$ do not satisfy the resonance conditions, Eq. (1), either. According to Longuet-Higgins [3] and McGoldrick *et al.* [14], a mismatch defined as $\delta k_5 = [|2\mathbf{k}_4 - \mathbf{k}_1| - (2\omega_4 - \omega_1)^2/g]/2 = -0.095$ and $\delta k_6 = [|2\mathbf{k}_4 - \mathbf{k}_3| - (2\omega_4 - \omega_3)^2/g]/2 = -0.31$ exists for the two degenerate sets, and the growth of the tertiary wave components $f_5 = 2f_4 - f_1 = 1.27$ Hz and $f_6 = 2f_4 - f_3 = 1.455$ Hz is given by

$$a_5 = \varepsilon_4^2 \varepsilon_1 \frac{G_5}{|\delta k_5|} |\sin(\delta k_5 d)|, \quad a_6 = \varepsilon_4^2 \varepsilon_3 \frac{G_6}{|\delta k_6|} |\sin(\delta k_6 d)|, \tag{16}$$

where $G_5 = G(r = f_4/f_1) = 1.31$ and $G_6 = G(r = f_4/f_3) = 1.01$ are the coupling coefficients for exact resonant interactions. According to Eq. (16), the amplitudes of f_5 and f_6 are periodic functions with $G_5/|\delta k_5| = 13.79$ and $G_6/|\delta k_6| = 3.26$ influencing their growth rate. Thus, the ratio of the maximum growth of f_5 to f_6 equals $4.23\varepsilon_1/\varepsilon_3$, which accounts for the rapid growth of f_5 in comparison to f_6 shown in Fig. 12. In addition, similar to the energy transfer in exact resonance, the energy of f_5 and f_6 in the degenerate quartets should not be directly transferred from $\mathbf{k}_1$, but contributed by $\mathbf{k}_4$, which would subsequently suppress the growth of $\mathbf{k}_4$ down-wave.

Figure 14 exhibits the contour plots of the normalized surface elevations $\eta/(a_1 + a_3)$ in the four cases listed in Table II, where the dashed line denotes the propagation direction of the resonant wave $\mathbf{k}_4$ and the squares are marked to compare the variations of wave patterns. It is observed that in C01 with $\varepsilon_1 = \varepsilon_3 = 0.03$, basically all the crest and trough lines are straight and regular. As the primary waves' steepness is increased to $\varepsilon_1 = \varepsilon_3 = 0.05$, although the crest and trough lines near the wavemaker boundaries still remain straight, they become curved further down-wave in the direction of $\mathbf{k}_4$. For increased steepness in C03 and C04, the crest lines at longer distances are shown to split into a longer segment with a larger wave crest and a shorter one with a smaller wave crest. The same phenomenon also occurs in the troughs. More explicitly, Fig. 15 shows the magnified evolution process of the crests. Through observation and comparison, it is found that the crest and trough lines' curvatures strengthen with an increase of the primary waves' steepness and the resonant wave's propagation distance.
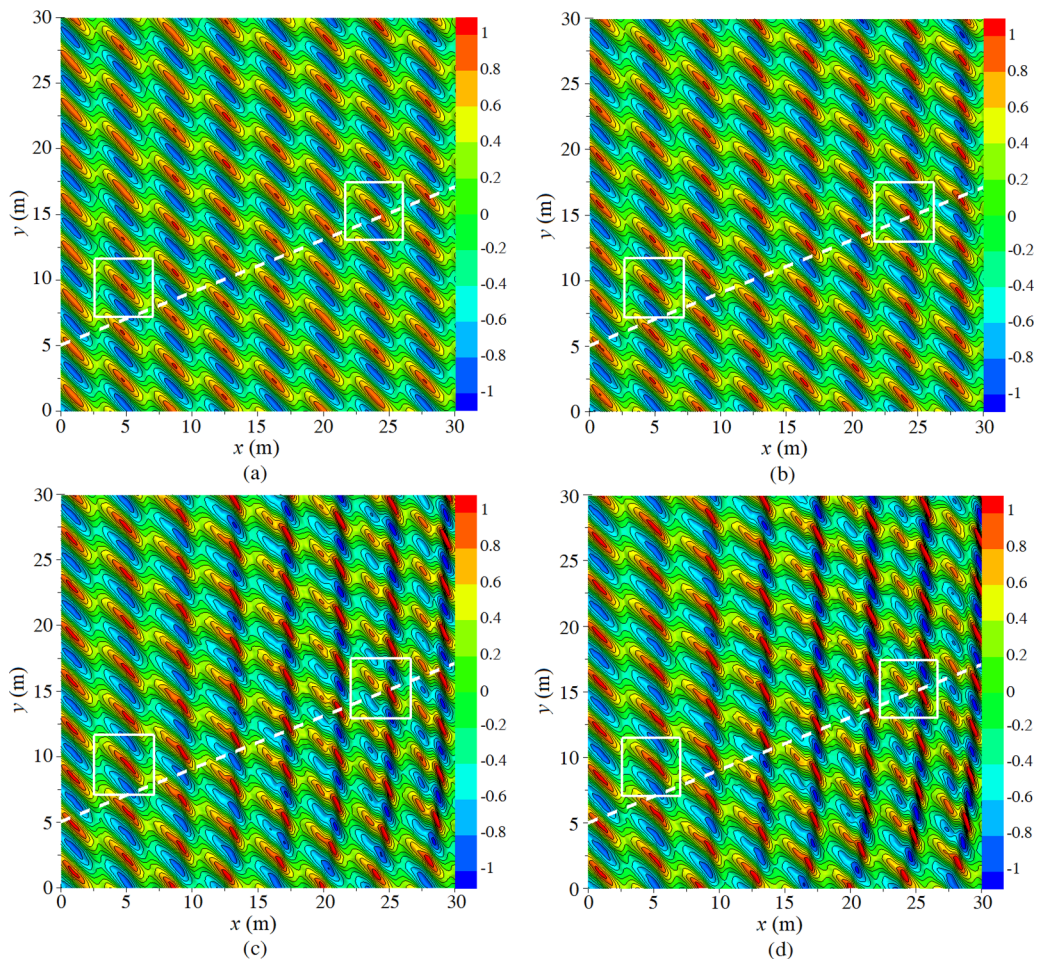
FIG. 14. Contour plots of the normalized surface elevations $\eta/(a_1 + a_3)$ at $t = 50$ s, where the dashed line denotes the propagation direction of the resonant wave $\mathbf{k}_4$: (a) C01, (b) C02, (c) C03, (d) C04.

In previous experimental studies of the third-order resonant interactions between two deep-water gravity waves, primary waves' steepness larger than 0.05 were studied (e.g., Refs. [14,16,17]), while the splitting phenomenon of the crests and troughs has never been shown. Nevertheless, Gibbs and Taylor [35] numerically investigated the spatial evolution of steep, directionally spread transient wave groups on deep water, and observed obliquely propagating "shoulders" or "wings" at the periphery of the wave group. The formation of such structure was attributed to energy transfer to high-wave-number components propagating at an angle to the mean direction, and the third-order resonant and quasiresonant interactions were responsible for the energy transfer. Subsequently, the growth-rate of the resonant components was calculated and found to agree well with the faster "dynamical" time-scale associated with quasiresonant interactions rather than the slower "kinetic" time-scale associated with exact resonant interactions [36]. The separated shorter wave crests shown in Figs. 14(c)–14(d) are similar to the "wing waves" observed in Refs. [35,36]. In the present study, the splitting of the crests and troughs is attributed to the resonant or quasiresonant interactions but requires further identification.

Due to the third-order resonant and quasiresonant interactions, there is an obvious energy transfer from the primary wave f_1 to high-frequency components f_4 and f_5 as observed in Fig. 12. Extracting
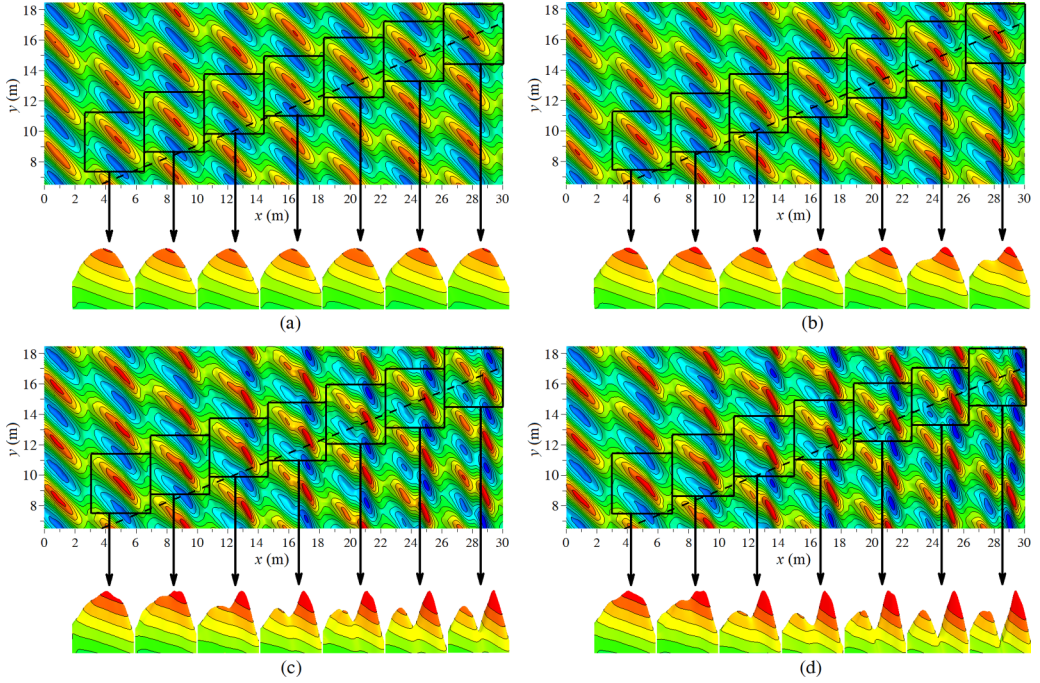
FIG. 15. Magnified evolution process of the crests: (a) C01, (b) C02, (c) C03, (d) C04.

the amplitudes of f_1, f_3, f_4, and f_5 from the amplitude spectra of C04 in Fig. 10 and then linearly superposing them, one obtains the five normalized wave patterns exhibited in Fig. 16. The upper one corresponds to the linear superposition of $\mathbf{k}_1$, $\mathbf{k}_3$, and $\mathbf{k}_4$ aiming to isolate the effect of the exact resonance on the variation of wave patterns in which the phase of the resonant wave $\mathbf{k}_4$ is locked to $-\pi/2$ with respect to the primary waves [3,16]. It is observed that with an increase of the propagation distance (i.e., with more energy transferred to the obliquely propagating high-frequency
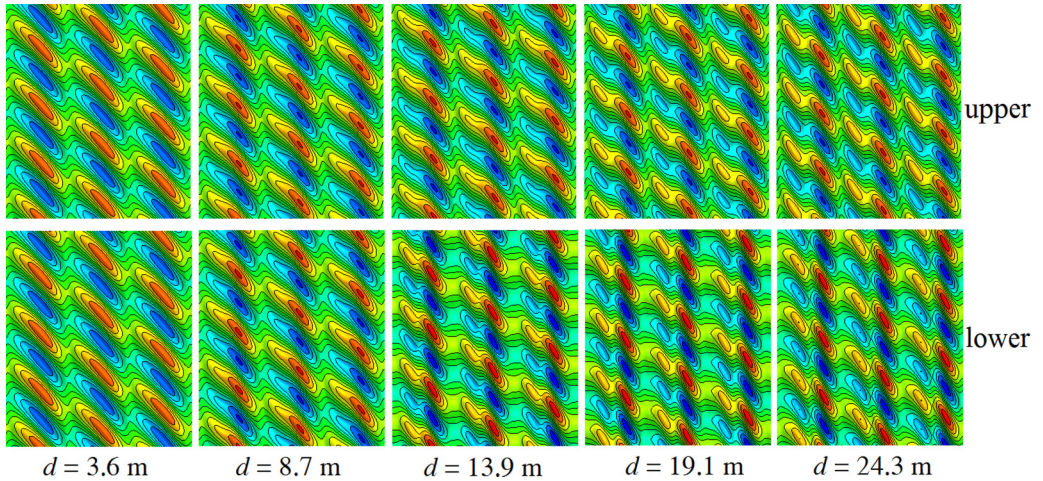

FIG. 16. Contour plots of the normalized surface elevations $\eta/(a_1 + a_3)$ obtained from the linear superposition of $\mathbf{k}_1 + \mathbf{k}_3 + \mathbf{k}_4$ (upper) and $\mathbf{k}_1 + \mathbf{k}_3 + \mathbf{k}_4 + \mathbf{k}_5'$ (lower).
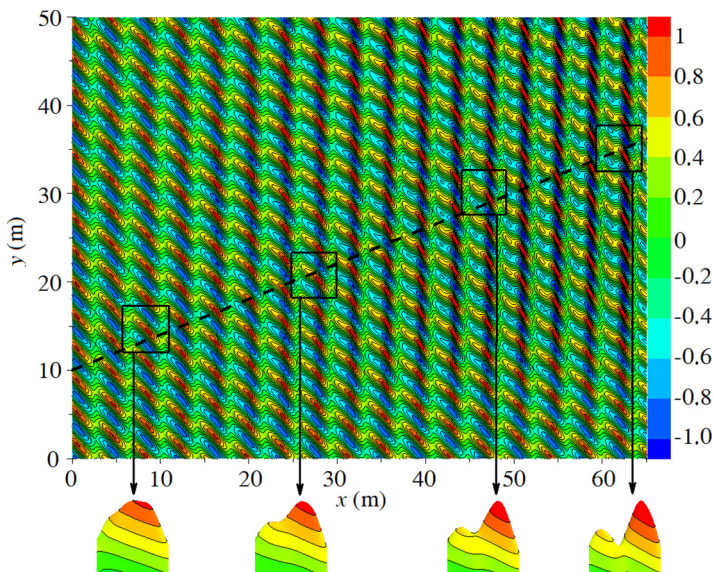
FIG. 17. Contour plot of the normalized surface elevations $\eta/(a_1 + a_3)$ in C02 at $t = 120$ s with an enlarged computational domain. The dashed line denotes the propagation direction of the resonant wave $\mathbf{k}_4$.

component f_4), the wave crest is first elongated, and then a small wave crest gradually lags behind and separates from the main crest as a result of the lower phase velocity of $\mathbf{k}_4$. The variations of the wave patterns turn out to be qualitatively consistent with the splitting process shown in Figs. 14(d) and 15(d). The lower portion of the figure corresponds to the superposition of $\mathbf{k}_5'$ (wave-number vector of f_5) intended to show the impact of the quasiresonance in which the phase of $\mathbf{k}_5'$ is locked to $2\mathbf{k}_4$ and $\mathbf{k}_1$. It is shown that the superposition of $\mathbf{k}_5'$ enhances the splitting extent and that the contour plots are quantitatively more similar to the splitting process shown in Figs. 14(d) and 15(d). However, the superposition of $\mathbf{k}_5'$ causes no essential change to the wave patterns. Hence, the bending and then splitting of the wave crests and troughs is actually attributed to the energy transferring from the primary wave $\mathbf{k}_1$ to the obliquely propagating high wave-number vector $\mathbf{k}_4$, which has a lower phase velocity in comparison to the primary waves as a result of exact resonant interaction. The subsequent quasiresonant interactions involving the resonant wave and the primary waves enhance the splitting extent without making essential changes to the wave patterns. Therefore, for primary waves with small steepness as in C01 and C02, if the propagation distance of the resonant wave is sufficiently large (i.e., with more energy transferred to obliquely propagating resonant wave $\mathbf{k}_4$), the crests and troughs will eventually split as in Figs. 14(c)–14(d). Hence, C02 is again simulated over an enlarged computational domain, 80 m long and 60 m wide, with the numerical parameters remaining unchanged. The simulated contour plot is shown in Fig. 17.

Figure 18 compares the time series of the nondimensionalized surface elevations $\eta/(a_1 + a_3)$ in cases C01–C04. It is shown that in the near propagation distance at $d = 3.6$ m, the nondimensionalized surface elevations in the four cases agree. However, as the propagation distance d increases, only the simulated results of C01 and C02 with small wave steepness show good agreement. Obvious discrepancies appear among C02, C03, and C04, and these inconsistencies become increasingly evident with the increase of the propagation distance. First, the phase difference among the four cases is larger with an increase of the propagation distance, which is caused by the evident growth of the wave components f_4 and f_5, together with the effect of amplitude dispersion. Then, with the increase of the primary waves' steepness, the maximum nondimensionalized wave crest becomes larger and more peaked, and its occurrence in C03 and C04 is clearly earlier than in C01 and C02 as indicated by t_{η_max} in this figure, which precisely corresponds to the separated larger
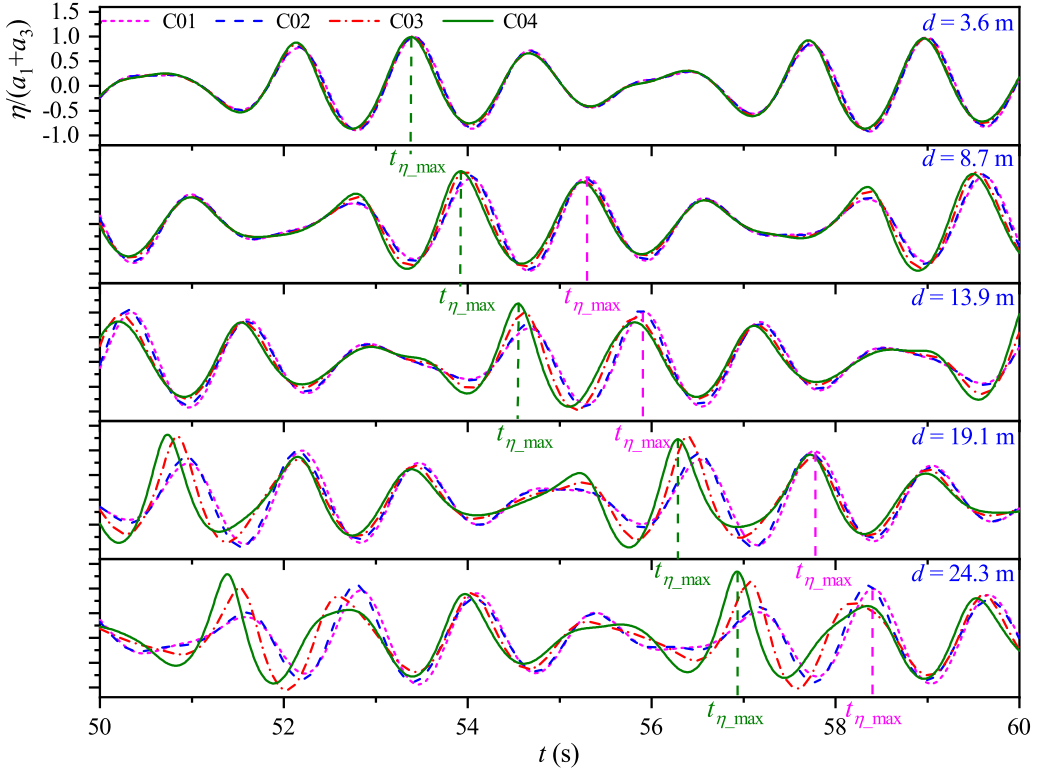
FIG. 18. Nondimensionalized surface elevations $\eta/(a_1 + a_3)$ at different propagation distances of the resonant wave $\mathbf{k}_4$ for C01, C02, C03, and C04, respectively.

wave crest as shown in Figs. 14 and 15. Furthermore, it is noticed that as the interactions propagate further, the surface elevations show obvious front-to-rear asymmetries in C03 and C04. It is well known that wave amplitude asymmetries and crescent shape deformations are characteristics of nonlinear wave groups due to four-wave quasiresonance [18,19]. That is why Fujimoto *et al.* [20] examined the degree of the asymmetry of the averaged freak wave shape to indicate the effect of the four-wave quasiresonance. Hence, the front-to-rear asymmetries of the surface elevations observed in Fig. 18 indicate the impact of the third-order quasiresonant interactions, which indirectly indicate that the frequency components f_5 and f_6 are generated from the quasiresonant interactions among the primary waves $\mathbf{k}_1$, $\mathbf{k}_3$ and the resonant wave $\mathbf{k}_4$.

Finally, the effect of the resonant interactions on velocity profiles is examined. Figure 19 compares the velocity profiles between the linear wave theory and the simulated results in C02 and C04, respectively. In this figure, the time at each propagation distance corresponds to the maximum wave crest of C04 as indicated in Fig. 18 (i.e., $t_0 = 53.38$ s at $d = 3.6$ m, $t_0 = 54.55$ s at $d = 13.9$ m and $t_0 = 56.93$ s at $d = 24.3$ m) and is expected. It is found that for primary waves with small steepness as in C02 ($\varepsilon_1 = \varepsilon_3 = 0.05$), as the resonant interactions are relatively weak, the linear wave theory works well within the computational domain, although some slight discrepancies are observed at $d = 24.3$ m caused by the continuous growth of the resonant wave $\mathbf{k}_4$. For primary waves with moderate wave steepness as in C04 ($\varepsilon_1 = \varepsilon_3 = 0.10$), because of the increased nonlinearity, some visible discrepancies are even observed at $d = 3.6$ m. Moreover, due to enhanced energy transfer as a result of intense resonant and quasiresonant interactions, the inconsistencies become increasingly evident as the nonlinear interactions evolve further. Since the selected time corresponds to the maximum wave crest of C04, the simulated vertical component w is approximately zero expectedly.
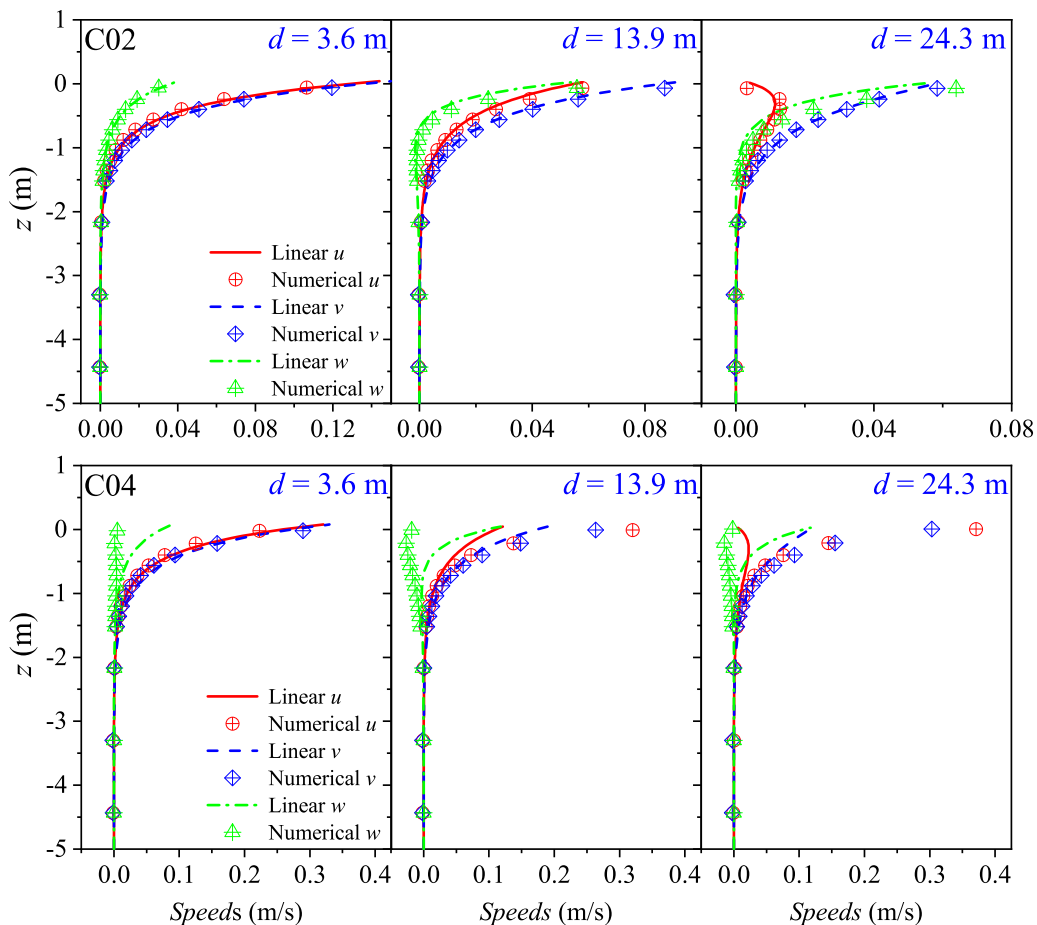
FIG. 19. Comparisons of the velocity profiles between the linear wave theory and the present numerical results in C02 and C04. (Note that there would be numerical speeds above mean water level, $z = 0$, only if $\eta > 0.16$ m, which is related to the vertical grid system but does not occur.)

It is noticed that the horizontal velocities at the maximum wave crest are shown to increase with the growth of the resonant wave's propagation distance. This corresponds to the increasingly peaked wave crest observed in Fig. 18. In the meantime, the velocity component u in the x direction evidently grows in comparison to the component v in the y direction and even exceeds the value of v for $d \geqslant 13.9$ m. It can be seen in Fig. 12 that the energy of the primary wave $\mathbf{k}_1$ with $\theta_1 = 32.45°$ decreases significantly with an increase in d, and that the energy of the primary wave $\mathbf{k}_3$ with $\theta_3 = 57.55°$ shows a slight gain. The growth of the velocity u in the x direction is attributed to the rapid growth of f_4 and f_5, with their propagation directions toward the positive x axis. Consequently, for primary waves with moderate steepness, the intense resonant and the subsequent quasiresonant interactions have such a profound influence on the velocity profiles that the velocity fields cannot be predicted from the linear predictions.

V. CONCLUDING REMARKS

The resonant interactions between two gravity wave trains in deep water are numerically studied using a 3D nonhydrostatic free surface flow model. First, five cases of nonresonant and resonant

interactions between two gravity wave trains are simulated and compared to known theories and experiments to test the reliability of the model. Then, four cases of resonant interactions are simulated and analyzed to study the effect of the primary waves' steepness on the evolutions of the tertiary resonant wave, three-dimensional wave patterns and velocity profiles.

As expected it is found that for primary waves with small steepness, the growth of the resonant wave could be predicted well by both the numerical results and the third-order theoretical predictions of Longuet-Higgins [3]. While for primary waves with moderate steepness, apparent discrepancies are observed at greater propagation distances, and the propagation distance or nonlinear distance of the resonant wave, within which the predictions of Longuet-Higgins [3] are accurate, decreases with the increase of the primary waves' nonlinearity. As is evident via spectral analysis, it turns out that the resonant interactions are sufficiently significant that the amplitude of one primary wave reduces substantially to transfer energy to generated tertiary wave components. This is actually inconsistent with the assumptions of Longuet-Higgins's resonance theory, which accounts for its overestimation of the resonant wave's growth.

Ever since the pioneering work of Phillips [2], the effect of resonant interactions in two dimensions has been studied extensively. However, less effort has been focused on three-dimensional wave patterns. Through numerical simulations, it is found here that for primary waves with small steepness, essentially all the crest and trough lines within the computational domain are straight and regular. As the wave steepness increases, the crests gradually become curved and then split into a longer segment with a larger wave crest and a shorter one with a smaller wave crest. Simultaneously, the curvature extent increases with the growth of the primary waves' steepness and the resonant wave's propagation distance. The same phenomenon also occurs in the troughs. Through analysis, it is identified that the bending and splitting of the crests and troughs are caused by the energy transfer from the primary waves to obliquely propagating high-frequency resonant wave with lower phase velocity due to exact resonance interaction. The subsequent quasiresonant interactions involving the resonant wave and the primary waves enhance the splitting extent. For primary waves with small nonlinearity, if the propagation distance is sufficiently large, i.e., with more energy transferred to obliquely propagating high-frequency resonant wave, the crest and trough lines will eventually split as well. Additionally, with an increase of the primary waves' nonlinearity, the maximum nondimensionalized wave crest down-wave is found to be larger and more peaked, and its occurrence is seen earlier. This precisely corresponds to the separated larger wave crest shown in the contour plots.

The effect of the resonant interactions on velocity profiles is investigated as well. By comparing the simulated results with the linear wave theory, it is shown as expected that for primary waves with small steepness, the linear wave theory roughly estimates the velocity profiles within the computational domain. For primary waves with moderate steepness, however, due to the significant resonant and quasiresonant interactions, the discrepancies between the linear and simulated results become increasingly evident as the nonlinear interactions evolve further. Besides, the horizontal velocities at the maximum wave crests increase as the interactions propagate, especially the velocity component in the x direction. Therefore, again as expected, the velocity fields can no longer be predicted from the linear theory.

[1] O. M. Phillips, Wave interactions—The evolution of an idea, J. Fluid Mech. **106**, 215 (1981).

[2] O. M. Phillips, On the dynamics of unsteady gravity waves of finite amplitude, J. Fluid Mech. **9**, 193 (1960).

[3] M. S. Longuet-Higgins, Resonant interactions between two trains of gravity waves, J. Fluid Mech. **12**, 321 (1962).

[4] D. J. Benney, Non-linear gravity wave interactions, J. Fluid Mech. **14**, 577 (1962).

[5] K. Hasselmann, On the non-linear energy transfer in a gravity-wave spectrum. Part 1. General theory, J. Fluid Mech. **12**, 481 (1962).

[6] K. Hasselmann, On the non-linear energy transfer in a gravity-wave spectrum. Part 2. Conservation theorems; wave-particle analogy; irreversibility, J. Fluid Mech. **15**, 273 (1963).

[7] K. Hasselmann, On the non-linear energy transfer in a gravity-wave spectrum. Part 3. Evaluation of the energy flux and swell-sea interaction for a Neumann spectrum, J. Fluid Mech. **15**, 385 (1963).

[8] F. P. Bretherton, Resonant interactions between waves: The case of discrete oscillations, J. Fluid Mech. **20**, 457 (1964).

[9] M. Tanaka, On the role of resonant interactions in the short-term evolution of deep-water ocean spectra, J. Phys. Oceanogr. **37**, 1022 (2007).

[10] R. S. Gibson and C. Swan, The evolution of large ocean waves: The role of local and rapid spectral changes, Proc. R. Soc. A **463**, 21 (2007).

[11] M. Onorato, A. R. Osborne, M. Serio, and S. Bertone, Freak Waves in Random Oceanic Sea States, Phys. Rev. Lett. **86**, 5831 (2001).

[12] P. A. E. M. Janssen, Nonlinear four-wave interactions and freak waves, J. Phys. Oceanogr. **33**, 863 (2003).

[13] M. S. Longuet-Higgins and N. D. Smith, An experiment on third-order wave interactions, J. Fluid Mech. **25**, 417 (1966).

[14] L. F. McGoldrick, O. M. Phillips, N. E. Huang, and T. H. Hodgson, Measurements of third-order resonant wave interactions, J. Fluid Mech. **25**, 437 (1966).

[15] H. Tomita, Theoretical and experimental investigations of interaction among deep-water gravity waves, Rep. Ship Res. Inst. **26**, 251 (1989).

[16] F. Bonnefoy, F. Haudin, G. Michel, B. Semin, T. Humbert, S. Aumaître, M. Berhanu, and E. Falcon, Observation of resonant interactions among surface gravity waves, J. Fluid Mech. **805**, R3 (2016).

[17] F. Bonnefoy, F. Haudin, G. Michel, B. Semin, T. Humbert, S. Aumaître, M. Berhanu, and E. Falcon, Experimental observation of four-wave resonant interaction: From low steepness to wave breaking, *Proceedings of the 32nd International Workshop on Water Waves and Floating Bodies*, Dalian, China, 23–26 April, 2017.

[18] E. Lo and C. C. Mei, A numerical study of water-wave modulation based on a higher-order nonlinear Schrödinger equation, J. Fluid Mech. **150**, 395 (1985).

[19] E. Lo and C. C. Mei, Slow evolution of nonlinear deep water waves in two horizontal directions: A numerical study, Wave Motion **9**, 245 (1987).

[20] W. Fujimoto, T. Waseda, and A. Webb, Impact of the four-wave quasi-resonance on freak wave shapes in the ocean, Ocean Dyn. **69**, 101 (2019).

[21] M. Onorato, A. R. Osborne, and M. Serio, Extreme wave events in directional, random oceanic sea states, Phys. Fluids **14**, L25 (2002).

[22] T. A. A. Adcock and P. H. Taylor, Fast and local non-linear evolution of steep wave-groups on deep water: A comparison of approximate models to fully non-linear simulations, Phys. Fluids **28**, 016601 (2016).

[23] G. Ducrozet, F. Bonnefoy, D. Le Touzé, and P. Ferrant, 3-D HOS simulations of extreme waves in open seas, Nat. Hazards Earth Syst. Sci. **7**, 109 (2007).

[24] A. Toffoli, O. Gramstad, K. Trulsen, J. Monbaliu, E. Bitner-Gregersen, and M. Onorato, Evolution of weakly nonlinear random directional waves: Laboratory experiments and numerical simulations, J. Fluid Mech. **664**, 313 (2010).

[25] A. Toffoli, M. Onorato, E. M. Bitner-Gregersen, and J. Monbaliu, Development of a bimodal structure in ocean wave spectra, J. Geophys. Res. **115**, C03006 (2010).

[26] G. Ma, F. Shi, and J. T. Kirby, Shock-capturing non-hydrostatic model for fully dispersive surface wave processes, Ocean Model. **43-44**, 22 (2012).

[27] C. Ai, S. Jin, and B. Lv, A new fully non-hydrostatic 3D free surface flow model for water wave motions, Int. J. Numer. Methods Fluids **66**, 1354 (2011).

[28] G. Stelling and M. Zijlema, An accurate and efficient finite-difference algorithm for non-hydrostatic free-surface flow with application to wave propagation, Int. J. Numer. Methods Fluids **43**, 1 (2003).

[29] M. Zijlema and G. S. Stelling, Efficient computation of surf zone waves using the nonlinear shallow water equations with non-hydrostatic pressure, Coastal Eng. **55**, 780 (2008).

[30] C. Ai and S. Jin, A multi-layer non-hydrostatic model for wave breaking and run-up, Coast. Eng. **62**, 1 (2012).

[31] C. Ai, W. Ding, and S. Jin, A general boundary-fitted 3D non-hydrostatic model for nonlinear focusing wave groups, Ocean Eng. **89**, 134 (2014).

[32] Y. Ma, C. Yuan, C. Ai, and G. Dong, Reconstruction and analysis of freak waves generated from unidirectional random waves, J. Offshore Mech. Arct. Eng. **142**, 041201 (2020).

[33] R. A. Dalrymple, Directional wavemaker theory with sidewall reflection, J. Hydraul. Res. **27**, 23 (1989).

[34] P. A. Madsen and D. R. Fuhrman, Third-order theory for bichromatic bi-directional water waves, J. Fluid Mech. **557**, 369 (2006).

[35] R. H. Gibbs and P. H. Taylor, Formation of walls of water in 'fully' nonlinear simulations, Appl. Ocean Res. **27**, 142 (2005).

[36] D. Barratt, H. B. Bingham, P. H. Taylor, T. S. van den Bremer, and T. A. A. Adcock, Directional energy transfer due to third-order interactions during an extreme wave event, *Proceedings of the 34th International Workshop on Water Waves and Floating Bodies*, Newcastle, Australia, April 7–10, 2019.